ORNL/TM-2023/2837

Microstructural Simulation of Ion Irradiated Natural Rocks and Minerals

Yann Le Pape
Mohammed Alnaggar

March 2023

OAK RIDGE National Laboratory

ORNL IS MANAGED BY UT-BATTELLE LLC FOR THE US DEPARTMENT OF ENERGY

ORNL/TM-2023/2837

Nuclear Energy and Fuel Cycle Division – NEUP 19-17747

MICROSTRUCTURAL SIMULATION OF ION IRRADIATED NATURAL ROCKS AND MINERALS

Yann Le Pape and Mohammed Alnaggar

March 2023

Prepared by
OAK RIDGE NATIONAL LABORATORY
Oak Ridge, TN 37831
managed by
UT-Battelle LLC
for the
US DEPARTMENT OF ENERGY
under contract DE-AC05-00OR22725

CONTENTS

LIST OF FIGURES v
ABBREVIATIONS vii
ABSTRACT 1
1. INTRODUCTION 1
2. MOSAIC 3
3. NEUTRON-IRRADIATION MODEL 4
   3.1 CRYSTAL ELASTICITY 4
      3.1.1 Pristine Properties 4
      3.1.2 Irradiated Properties 4
   3.2 RADIATION-INDUCED EXPANSION 5
      3.2.1 Volumetric Change 5
      3.2.2 Anisotropy 5
   3.3 ISOTROPIC DAMAGE 5
4. CONSIDERATION OF ION IRRADIATION 6
   4.1 IRRADIATION DAMAGE 6
   4.2 RADIATION-INDUCED EXPANSION 7
   4.3 MECHANICAL STRESSES IN THE ION-IRRADIATED FILM 9
   4.4 HYPOTHESIS ABOUT MECHANICAL INTERACTION DURING ION-IRRADIATION . 10
      4.4.1 Thermal Expansion 10
      4.4.2 Phase Transition 10
      4.4.3 Crystalline Plasticity 10
5. IRRADIATION-INDUCED FLOW 11
   5.1 PLASTICITY-BASED MODEL 11
   5.2 GEOMETRY AND INPUTS FOR THE SIMULATION OF ION IRRADIATION 12
   5.3 DISCUSSION OF SIMULATION RESULTS 13
      5.3.1 Boundary Restraints from the Nonirradiated Material 13
      5.3.2 Stress-Induced Plastic Flow 15
      5.3.3 Amorphization Effect on Yield Strength 16
      5.3.4 Specimen Geometry 17
      5.3.5 Possible Additional Interactions 17
6. IRRADIATION SIMULATIONS WITH MOSAIC 19
   6.1 PHASE MAPS 19
   6.2 NEUTRON IRRADIATION 19
   6.3 ION IRRADIATION 19
7. CONCLUSIONS 23
8. REFERENCES 25

LIST OF FIGURES

1 Displaced atom profiles with increasing fluence (top), volumetric expansion profiles (middle), and step height evolution with increasing fluence assuming either a redistribution of the volumetric expansion in the vertical direction (i.e. $\varepsilon_z^* = \varepsilon^*$ and $\varepsilon_x^* = \varepsilon_y^* = 0$ – black dots connected by a solid line) or isotropic expansion (black hollow marks connected by a dashed line), red hollow marks: [15] data (bottom). 8

2 dpa profile under different irradiation energies and fluences computed using SRIM simulations. 12

3 Full mesh of the irradiated disc (left), mesh for one quarter of the disc showing symmetry boundary conditions (middle), and mesh refinement over depth (right). 13

4 Stress distributions over the irradiated film depth: (a) σ_{XX}, (b) σ_{YY}, (c) σ_{ZZ}, and (d) σ_{VM}. . . 14

5 Shear stress over a vertical section through the irradiated film (left), and formation of ridges around the irradiated window (right). 15

6 Strain distributions over the irradiated film depth: (a) ε_{XX}, (b) ε_{YY}, (c) RIVE, and (d) -RIVE/3. 16

7 Step height obtained by integrating ϵ_{ZZ} over the height 17

8 Bottom curvature at (a) 3×10^{14} ion.cm^{-2}, (b) 6×10^{15} ion.cm^{-2}, (c) 8×10^{15} ion.cm^{-2}, and (d) 1×10^{16} ion.cm^{-2} 18

9 Top displacement around irradiated window. 18

10 Phase maps of anorthite (left), and granite (right) specimens showing the slices used in MOSAIC simulations. 20

11 Elastic stress state within (a) anorthite sample and (b) granite sample at full amorphization with free boundary conditions to represent neutron irradiation: maximum principal stress (left), minimum principal stress (middle), and Von Misses stress (right). . . . 21

12 Elastic stress state within (a) the anorthite sample and (b) the granite sample at full amorphization with fixed boundary conditions to represent ion irradiation: maximum principal stress (left), minimum principal stress (middle), and Von Misses stress (right). . . . 22

ABBREVIATIONS

DOE	US Department of Energy
dpa	displacements per atom
EDXS	energy-dispersive x-ray spectroscopy
FFT	fast-Fourier transform
GB	grain boundary
IMAC	Irradiated Minerals, Aggregates and Concrete
IPI	interparticle interface
LWR	light-water reactor
LWRS	Light-Water Reactor Sustainability
MCNP	Monte Carlo N-particle
MD	molecular dynamics
MOSAIC	Microstructure-Oriented Scientific Analysis of Irradiated Concrete
MR	Materials Research
mXRF	micro x-ray fluorescence
NPP	nuclear power plant
ORNL	Oak Ridge National Laboratory
RIVE	radiation-induced volumetric expansion
SLR	subsequent license renewal
SRIM	Stopping and Range of Ions in Matter
XRD	x-ray diffraction

ABSTRACT

This report details the contribution of Oak Ridge National Laboratory to the Nuclear Energy University Program (NEUP) project, "Rapid Characterization of Concrete Mineralogy using Multi-Scale Tools" led by the University of Illinois at Urbana-Champaign. To support the subsequent license renewal (SLR) of the US nuclear power plants (NPPs) fleet, the performance of concrete-forming aggregates against neutron irradiation needs to be assessed. Ion irradiation is proposed as a rapid, cost-effective surrogate method to full neutron irradiation testing. To complement the characterization of ion-irradiated rock specimens, ORNL has run finite-elements and fast-Fourier transform (FFT-based) simulations using the codes MARS and Microstructure-Oriented Scientific Analysis of Irradiated Concrete (MOSAIC). The main conclusion of this analysis is that the apparent post–ion-irradiation step-height underestimates the accumulated free radiation-induced volumetric expansion (RIVE) in the ion-implanted depth by about 15% at full amorphization and about 25% toward the beginning of the ion irradiation experiment. The discrepancy is explained by the fact that the step height is proportional to the sum of the RIVE (i.e., one third of the RIVE) and the irradiation-assisted plastic strains in the vertical direction (lower than two thirds of the RIVE). Because of the large lateral compressive stresses caused by the restraining effect of the unirradiated substrate, the stress field in the mineral grains and at the grain boundary (GB) in the ion-implanted layer is much different than the comparable stress field occurring during neutron irradiation. Hence, the mismatch RIVE causing cracks in the rock-forming minerals leads to different cracking patterns. Ion irradiation continues to be used as a rapid technique to assess the RIVE potential of rocks.

1. INTRODUCTION

The US DOE Light-Water Reactor Sustainability (LWRS) Program Materials Research (MR) Pathway aims at developing knowledge, methodologies and tools to inform subsequent license renewal (SLR) of nuclear power plants (NPPs). Concrete aging under prolonged exposure to irradiation, moisture ingress, and super-ambient temperature in critical and safety-related structures (biological shield and containment building) requires developing generic rapid-assessment tools accounting for the specificities of the concrete used in NPPs. To this aim, the LWRS Program has developed a unique software named MOSAIC (Microstructure Oriented Scientific Analysis of Irradiated Concrete). External collaboration is needed to strengthen MOSAIC's capabilities and to validate the modeling approach. The background of the NEUP RC-10.1 "Rapid, Multi-Modal Characterization of Concrete's Degradation Tolerance in Support of Second License Renewals of Nuclear Power Plants," is aligned with this objective. Hence, ORNL is a contributing partner of the project entitled "Rapid Characterization of Concrete Mineralogy Using Multi-Scale Tools" led by the University of Illinois at Urbana-Champaign. This project includes three main objectives:

1. Task 1: Characterization of ion radiation response of pure minerals relevant to concrete aggregates,
2. Task 2: Development of a rapid multi-modal characterization protocol for pristine and ion-irradiated minerals and rock, and,
3. Task 3: Implementation of characterization data into a micromechanical model.

This technical report addresses Task 3. The underlying motivation for this work is as follows: Could ion-irradiation experiments provide an alternative method to assess concrete's tolerance of neutron irradiation? To address this question, the method presented in this report includes describes the current capabilities of the MOSAIC (Microstructure-Oriented Scientific Analysis of Irradiated Concrete) code to model the effects of neutron-irradiation. This is followed by a discussion of the difference between neutron

and ion irradiation and an analysis of how MOSAIC's capabilities were extended to account for ion irradiation–assisted plasticity. MOSAIC outputs are compared for both types of irradiation on the same microstructures.

Nota Bene: ORNL has been contributing to two parallel NEUP projects addressing topic RC-10.1 "Rapid, Multi-Modal Characterization of Concrete's Degradation Tolerance in Support of Second License Renewals of Nuclear Power Plants" with similar general objectives:

1. "Rapid Characterization of Concrete Mineralogy Using Multi-Scale Tools" led by the University of Illinois at Urbana-Champaign (this report), and,
2. "Integrating multi-modal microscopy techniques and the MOSAIC simulation environment to assess changes in the physical properties and chemical durability of concrete following radiation exposure" led by the University of California at Los Angeles (report ORNL/TM-2023/2838 "Significance of Ion-Irradiated Natural Aggregates for Light-Water Reactor Subsequent License Renewal").

Varied rocks mineralogy and characterization methods were studied in these two projects. However, the simulation methodology is identical for both project. Thus, for the sake of readability and to create a comprehensive document, Sections 2 through 4 are integrally reproduced from the report ORNL/TM-2023/2838.

2. MOSAIC

MOSAIC—Microstructure-Oriented Scientific Analysis of Irradiated Concrete—is a simulation software developed for the US Department of Energy (DOE)Light-Water Reactor Sustainability (LWRS) Program. Using fast-Fourier transform (FFT)–based simulation methods [20, 21, 11], MOSAIC makes it possible to run efficient mechanical simulations of complex microstructures and to derive their effective mechanical behavior assuming periodic boundary conditions. The capabilities of MOSAIC are fully described in the paper by Torrence et al. [26]. The current maximum pixel size of a 2D microstructure is limited to 1,024 × 1,024. The physical dimensions of a pixel depends on the phase imaging methods. In practice, MOSAIC generally uses micro x-ray fluorescence (mXRF) characterization as a primary means of generating the microstructure. The corresponding pixel size is thus limited by the resolution of the mXRF instrument of about ≈ 15 μm. In practice, such a pixel size is sufficient to represent many rock assemblages although it may be limited to adequately represent fine grain structures (i.e., micro-crystalline, aphanitic igneous rocks). Microstructure generation using combined optical microscopy, x-ray diffraction, energy-dispersive x-ray spectroscopy, and mXRF is described in Li et al. [14]. However, there is virtually no limit on the characterization methods as long as the selected technique or combination of techniques makes it possible to identify the local mineral phases with a certain degree of confidence. In this research, the phase maps are generated by the University of Illinois at Urbana-Champaign using Raman spectroscopy. The process for modeling complex rock microstructures with MOSAIC follows one of two distinct strategies:

1. Each pixel is associated with a specific mineral phase. In this case, adjacent pixels are strictly bonded for continuity of the stress and displacement fields. This approach accounts for local heterogeneities at the scale of the pixels, but the continuity of the mechanical field does not permit representation of the local displacement discontinuities caused by cracking.

2. Groups of adjacent pixels with comparable mineral compositions are categorized into so-called *particles*. This approach allows for generation of larger crystals with unique crystalline orientations and identification of the crystal's boundary. The boundary between two adjacent particles is materialized by a one-pixel layer called the *interparticle interface* (IPI). Because of its non-zero thickness, the IPI represents two layered phases and their interface properties. In practice, identification of the IPI properties is difficult, so the modeling strategy must resort to averaging the IPI properties in accordance with the effective properties of the entire microstructure.

Once the phase map generation is completed, nonlinear mechanical simulations of the studied domain can be run in MOSAIC. MOSAIC is linked to the Irradiated Minerals, Aggregates and Concrete (IMAC) database which was developed for the LWRS program. The IMAC database includes data on physical and mechanical properties for a variety of common rock-forming minerals that are used as material inputs in MOSAIC simulation. This feature allows for consistency when simulating various rocks and concrete. The properties and constitutive models included in the most recent MOSAIC release are described in the following section.

3. NEUTRON-IRRADIATION MODEL

3.1 CRYSTAL ELASTICITY

3.1.1 Pristine Properties

The variety of minerals forming a rock's assemblage is vast and depends on the rock's genesis and subsequent transformation and weathering. Currently, the IMAC database only contains 43 minerals, corresponding to approximately 120 Mb of source code files, portable document format (pdf) documentation, and 72,000 lines of extensible markup language (XML) output data. The number of imported minerals may seem low compared to the >4,500 different known minerals. However, this database is oriented toward concrete aggregate. In that regard, more than 90% of the minerals on Earth's the crust are composed of silicate minerals. The most abundant silicates are feldspars: plagioclase (~40%) and alkali feldspar (~10%). Other common silicate minerals are quartz (~10%), pyroxenes (~10%), amphiboles (~5%), micas (~5%), and clay minerals (~5%) [28]. The remainder of the silicate family comprises 3% of the crust. Only 8% of the crust is composed of nonsilicates such as carbonates, oxides, and sulfides. Although the IMAC database may be expanded in the future, to a large extent, the current list of minerals covers concrete aggregate–forming minerals. Minerals currently available in IMAC are albite, analcime, andesine, ankerite, anorthite, anorthoclase, augite, biotite, bromellite, bronzite, bytownite, calcite, cassiterite, chamosite, clinochlore, cordierite, corundum, diopside, dolomite, enstatite, fluorapatite, forsterite, hematite, hornblende, hydroxylapatite, labradorite, lizardite, magnesite, magnetite, microcline, muscovite, nepheline, oligoclase, orthoclase, periclase, phlogopite, pyrope, quartz, rutile, sanidine, siderite, silica (amorphous), and spinel. Because natural mineral compositions are subject to atom substitutions, they cannot be taken into account unless thorough characterizations associated with first-principle simulations are conducted. Except for alkali-feldspars and plagioclase ranked into broad categories (e.g., labradorite, bytownite,. . .), only pristine mineral compositions are considered. The variety of crystalline structures necessitates descriptions of the minerals' elastic properties with generally anisotropic stiffness tensors. The number of individual elastic constants varies with the crystalline structure. These constants can be identified from experimental testing or first-principle simulations. A thorough literature search revealed that a collection of minerals' elastic properties is included in the IMAC database. The number of data per constant varies with the type of mineral (14 for quartz, the most studied mineral). In MOSAIC simulations, it is assumed that the pristine elastic constants are given by the average values of the collected data. The stiffness tensors of the most common rock-forming minerals can be found in the appendix of a paper by Le Pape and Sanahuja [13].

3.1.2 Irradiated Properties

Neutron irradiation–induced distortion of the minerals' crystal network affects their chemical, physical, and mechanical properties. As a result of this amorphization, minerals evolve toward a more isotropic system. The evolution of the minerals' individual elastic constants has not been studied sufficiently. The only experimental data available in the public literature were obtained on neutron-irradiated quartz in the late 1960s [17, 18]. Individual elastic constants of irradiated quartz exhibit either monotonic or nonmonotonic evolution. The stiffness tensor evolves toward an isotropic tensor that differs from amorphous silica. Molecular dynamics (MD) simulations were used to analyze the irradiated stiffness tensors of albite, almandine, anorthite, diopside, enstatite, janeite, nepheline, and quartz [10]. At full amorphization, the elastic constants of quartz obtained by MD match the experimental data published by Mayer et al. [17, 18] Interestingly, the equivalent Young's moduli (E) of the polycrystalline assemblages

made of a single mineral appear to be correlated with the change of density (ρ) caused by irradiation—$E^*/E_0 \approx (\rho^*/\rho_0)^3$—with $_0$: pristine properties, *: irradiated properties. At the current stage of MOSAIC developments, and because of the lack of data on irradiated elastic properties, the irradiated minerals' stiffnesses are assumed constant.

3.2 RADIATION-INDUCED EXPANSION

3.2.1 Volumetric Change

RIVE is the main mechanism caused by neutron irradiation. Few minerals exhibit shrinking under neutron bombardment, such as vitreous forms of silica. There is growing evidence that anorthite (calcium-bearing feldspar) shrinks, whereas albite (sodium-bearing feldspar) expands [10]. The RIVE rate and final amplitude vary with the chemical composition, the ratio of covalent-to-ionic bonds, and the silica content [12]. Empirical RIVE models are proposed in the literature [30, 1, 12]. RIVE of silicates tends to follow sigmoidal behaviors. Using the post-irradiation RIVE published in the Russian literature [3], best-fit parameters were derived for a series of empirical RIVE models applied to broad categories of minerals: carbonates, feldspars, pyroxenes, micas, and so on [12].

3.2.2 Anisotropy

Radiation-induced volumetric changes do not occur isotropically [3]: the elongation along the a-axis tends to be higher than along the b- and c-axes. Denisov et al. found that most minerals have a quasi-linear relationship between the lattice parameter changes and the volume change for a large range of neutron fluence [3]. Therefore, MOSAIC provides the option to distribute the RIVE along the crystal axis to account for anisotropy without modifying the volumetric swelling. By default, the redistribution coefficients were calibrated using Denisov's data. However, those data are questionable for the highest RIVE values associated with a complete amorphization of the originally pristine crystal structure, resulting in isotropization of the minerals [23]. In MOSAIC, the anisotropy of the volumetric change can be taken into account through a constant redistribution tensor. Cheniour et al. [2] found that the role of RIVE anisotropy on the effective properties of irradiated rocks is predominant when the composition of the rocks is mainly homogeneous, such as in quartzite.

3.3 ISOTROPIC DAMAGE

MOSAIC includes an isotropic damage model with linear softening. In previous studies [2], the use of the implemented damage model was limited to the IPIs. The underlying assumption is that cracking occurs mainly at the mineral GBs. This hypothesis is questionable in the light of recent characterization work being conducted at ORNL. Irradiated aggregates appears to exhibit intra-, inter-, and trans-granular cracking.

4. CONSIDERATION OF ION IRRADIATION

Any electromagnetic or particulate irradiation interacting with matter causes a flux attenuation. Neutron attenuation in concrete and concrete-forming aggregates exposed to the light-water reactor (LWR) spectrum is on the order of a factor of 4–5 over the first 0.1 m of the biological shield facing the reactor cavity [4]. At the scale of a concrete-forming aggregate (size $<\approx$ 25 mm), the neutron flux attenuation is thus quite limited. Hence, rock-forming minerals are subject to a neutron flux that can be considered homogeneous. Aggregate specimens subject to neutron irradiation in test reactors tend to be exposed to relatively uniform flux. Assuming that aggregates can be reasonably described as randomly oriented polycrystalline assemblages, the effective mechanical behavior of neutron-irradiated aggregates is isotropic: dimensional change [16] or irradiated elastic and strength properties.

In contrast, high-energy ions are rapidly stopped when penetrating matter. The penetration range varies with the type of ion and the irradiation energy, but it remains limited to a layer of a few micrometers in reality. Within the penetration range, ion stoppage is not uniform. The ion flux across the penetration depth the tends to have the shape of a log-normal distribution, with a peak located toward the the maximum penetration depth. Hence, the irradiation exposure and their effects on the local material properties are nonuniform.

The objective of this study is to analyze the effects of ion irradiation on the physical and mechanical properties of rock-forming minerals and rocks and to assess the representativeness of ion irradiation as a surrogate to neutron irradiation. The proposed method is based on the hypothesis that displacements per atom is an effective measure of irradiation-induced damage independently of the particle used for the experiment. This hypothesis makes it possible to find a relation between the ion dose and the change of density in the irradiated material.

4.1 IRRADIATION DAMAGE

In this study, the displacements per atom were obtained from the irradiation simulation code SRIM: Stopping and Range of Ions in Matter. Kinchin and Pease (K-P) models [8] were used to calculate the SRIM profiles and estimate the irradiation induced displacement per atom (DPA) in our study. Previous studies by Stoller et al. [24] and Saha et al. [27] recommend the use of K-P models to compute dpa from an ion irradiation experiment for comparison with results of neutron or other ion irradiation experiments. These studies found the dpa generated using the K-P model to be comparable with the Norgett-Robinson-Torrens (NRT) model [19], which is typically used as a standard to assess radiation damage effects in fast reactor materials.

Stopping and Range of Ions in Matter (SRIM) profiles are provided as displaced atoms per volume per ion fluence: $da/v \times \phi$ (in nm^{-1} [15], where v the volume and ϕ is ion fluence [29]. However, neutron irradiation results are provided in displacements per atom (dpa) by the fraction of displaced atoms per the total number of atoms. Both are related as follows:

$$dpa_\iota = \frac{da}{\mathcal{N}\rho v/M} \times \phi, \tag{1}$$

where $\mathcal{N}$ is Avogadro's number ($6.02214076 \times 10^{23}\ \mathrm{mol}^{-1}$), ρ is density ($\mathrm{g\,cm}^{-3}$), and M is molecular weight ($\mathrm{g\,mol}^{-1}$).

For a given reactor spectrum and a given mineral composition, the corresponding dpa can be estimated from the neutron fluence Φ by radiation transport models (e.g., MCNP):

$$dpa_n = \kappa \times \Phi, \tag{2}$$

where κ is a constant for a specific mineral and a specific neutron energy spectrum.

Analysis of the Russian reactors AM, BR-5 (OK-50), BR-5 (M-1), BR-10 (OK-70) and BOR-60 VEK (ORNL) shows that κ ranges between 1.4×10^{-22} and 5.8×10^{-22} dpa/(n.cm^{-2}). Hence, a dose of 0.1 dpa requires at least an integrated neutron fluence of 1.7×10^{20} n.cm^{-2}. The ratio of fluence at energy $E > 10$ keV against the integrated fluence is noted as ξ. Under 10 keV, the neutron energy is considered too low to produce damage in rock-forming minerals [1, 3].

The main hypothesis in this work is that equations (1) and (2) can be related: $\boxed{dpa_\iota \sim dpa_n}$.

4.2 RADIATION-INDUCED EXPANSION

Neutron-induced expansions of minerals are estimated using empirical models [12] based on Russian data [3] gathered in ORNL's IMAC database: $\varepsilon^* = f(\Phi, T)$, where Φ is the neutron fluence, Φ, in n.cm^{-2} at $E > 10$ keV (damaging neutrons in rock-forming minerals).

Hence, combining equations (1) and (2), the equivalent volumetric expansion at depth z reads as follows:

$$\tilde{\varepsilon}^*(z) = f\left(\frac{1}{\kappa}\frac{Mda(z)}{\rho \mathcal{N}} \times \xi\phi, T_{amb}\right), \tag{3}$$

where T_{amb} is the ambient temperature: it is assumed that the ion irradiation–induced heating is dissipated by convection.

An initial interpretation of the step height measurement can be obtained by integrating Eq. (3) over the implanted depth. It is assumed that there are no mechanical interactions caused by the restrained expansion in this analysis. The results are presented in Figure 1. The profiles of displaced atoms per unit volume evolve proportionally with the ion dose. The RIVE profiles are obtained using Eq. (3) assuming that quartz expansion is governed by Zubov's sigmoidal model [30] (see parameters in [12]). The shapes of the RIVE profiles are similar to those of the displaced atoms profiles until the maximum expansion is reached first at the depth where the dpa is at its highest at ≈ 2 μm. This occurs between 0.5×10^{14} and 1×10^{14} ion.cm^{-2}, which is slightly below the amorphization fluence estimated at 2×10^{14} ion.cm^{-2} or the transmission electron microscope diffraction pattern analysis [15]. At higher fluences, the region of maximum RIVE expands in the z direction and reaches the top surface for fluences $\geq 1 \times 10^{15}$ ion.cm^{-2}. The experimental step height measurements appear to coincide with the expansions calculated. Assuming that RIVE remains isotropic for fluence values under 2×10^{13} ion.cm^{-2}, the experimental step height increases rapidly. At $\approx 5 \times 10^{15}$ ion.cm^{-2}, the measured step height is comparable to the calculated step height assuming a full redistribution of the expansions in the vertical direction.

In summary, the change of density integrated over the irradiation penetration range cannot solely explain the step height observed after ion irradiation. When the implanted depth is fully amorphized, it is consistently observed that the step height divided by the penetration depth, which is the average deformation along the direction of the ion beam, is comparable to the neutron irradiation-induced

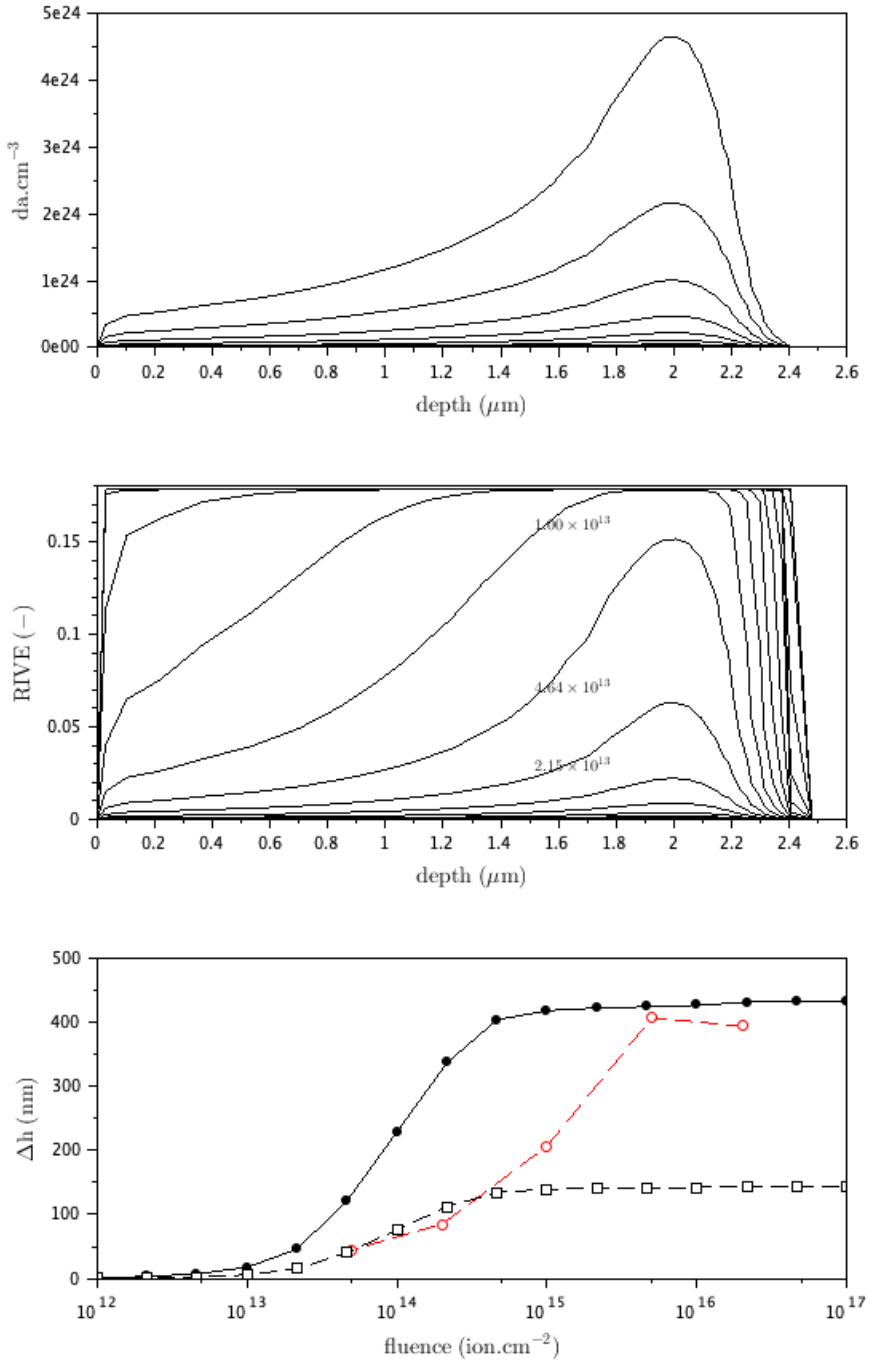

Figure 1. Displaced atom profiles with increasing fluence (top), volumetric expansion profiles (middle), and step height evolution with increasing fluence assuming either a redistribution of the volumetric expansion in the vertical direction (i.e. $\varepsilon_z^* = \varepsilon^*$ and $\varepsilon_x^* = \varepsilon_y^* = 0$ – black dots connected by a solid line) or isotropic expansion (black hollow marks connected by a dashed line), red hollow marks: [15] data (bottom).

volumetric expansion, or the cumulative contribution of the dimensional change in all directions [5, 23, 15]. Thus, it can be inferred that during ion irradiation, mechanical interactions affect radiation-induced expansion. It has been hypothesized that a mechanism described as a "radiation enhanced plastic flow" or a "viscous flow" exists during ion irradiation [25, 6]. Because the expansion of the irradiated film is constrained by a thick unirradiated substrate, the development of stresses in the film is inevitable.

4.3 MECHANICAL STRESSES IN THE ION-IRRADIATED FILM

The objective of this section is to provide the order of magnitude of the expected stresses that develop in the ion penetration depth. The following simplifying assumptions are made:

1. No lateral deformation: $\vec{u} = u_z(z) \cdot \vec{e}_z$; $\varepsilon_x = \varepsilon_y = 0$
2. Pristine isotropic elastic properties prevail through the thickness of the irradiated zone.

Navier's equations read as follows: [*]:

$$\frac{\partial^2 u_z(z)}{\partial z^2} = \frac{K}{M}\frac{\partial \varepsilon^*(z)}{\partial z}, \tag{4}$$

where K is the P-wave modulus and M is the bulk modulus. By integration, the mechanical strains in the vertical directions read as follows:

$$\varepsilon_z(z) = \frac{K}{M}\varepsilon^*(z). \tag{5}$$

In Hooke's equation using Lamé's first elastic constant λ and the shear modulus μ, the lateral stresses lead to: $\sigma_x = \sigma_y = \lambda\varepsilon_z$. The vertical stresses are given by: $\sigma_z = (\lambda + 2\mu)\varepsilon_z$. Hence, the average lateral pressure in the irradiated depth is given by

$$\langle\sigma_l\rangle = \frac{1}{\delta}\int_0^\delta \frac{\lambda K}{M}\varepsilon^*(z)dz = \frac{\lambda K}{M}\frac{\beta\Delta h}{\delta}, \tag{6}$$

where δ the ion penetration depth. β is an adimensional parameter description of the apparent redistribution of irradiation-induced volumetric expansion in the vertical direction: $\beta = (1/\Delta h)\int_0^\delta \varepsilon^*(z)dz$. The lateral stress in the implanted quartz is calculated assuming $E = 112$ GPa and $\nu = 0.08$ (polycrystallin assumption): $\lambda = E\nu/(1+\nu)/(1-2\nu) = 9.9$ GPa, $M = E(1-\nu)/(1+\nu)/(1-2\nu) = 113.6$ GPa and $K = E/3/(1-2\nu) = 44.4$ GPa, $\max(\varepsilon^*) \sim 0.18$: $\max\langle\sigma_l\rangle \sim 9.9 \times 44.4/113.6 \times 0.18 \sim 0.7$ GPa.

At these stress levels, the assumption of infinitesimal strains starts becoming quite questionable. For example, at $p \simeq 1$ GPa, the isothermal equation of state for quartz leads to a volume change of $\approx 2.5\%$ [22]. However, that volume change is not very different from the linear approximation of $1/K_0 \approx 2.7\%$.

The other factor that would affect the elastic analysis is the irradiation-induced softening of the elastic properties of minerals. Whereas limited data are available in the open literature [17, 18], it is acknowledged that a reasonable approximation of irradiation of the elastic bulk modulus is given by $K_*/K_0 \simeq (\rho^*/\rho_0)^3$ [10], where K^* is the irradiated bulk modulus, and is the pristine bulk modulus. Similar notations are used for the pristine and bulk densitie:. at maximum RIVE, $K^*/K_0 \simeq 0.612$. Thus, this softening leads to a reduction of the lateral pressure of about 40%, but it will not affect Eq. (5) because $K^*/M^* \simeq K_0/M_0$.

[*] $\mu\nabla^2\vec{u} + (\lambda+\mu)\nabla\cdot(\nabla\vec{u}) = \varpi\varepsilon^*/3$ with $\varpi = 3\lambda + 2\mu$ (thermal analogy). Since $\vec{u} = u_z(z)\cdot\vec{e}_z$, $\nabla\cdot(\nabla\vec{u}) = (\lambda+\mu)\partial^2 u_z/\partial z^2$.

In summary, when mechanical interactions during ion irradiation are assumed to be limited to elastic effects, the cumulative vertical expansion reads as follows:

$$\delta\langle\tilde{\varepsilon}_z\rangle = \int_0^\delta \left(1 + \frac{K_0}{M_0}\right)\varepsilon^*(z)dz \simeq 1.39 \int_0^\delta \varepsilon^*(z)dz. \tag{7}$$

Experimentally, the measurement of the vertical expansion at full amorphization is close to $3\int_0^\delta \varepsilon^*(z)dz$. In conclusion, a sole elastic mechanical interaction cannot explain the amplitude of the post–ion irradiation step-height measurement.

4.4 HYPOTHESIS ABOUT MECHANICAL INTERACTION DURING ION-IRRADIATION

4.4.1 Thermal Expansion

The coefficients of thermal expansion of α-quartz vary quasi linearly between 13–16 $\mu m\, m^{-1}\, °C^{-1}$ (a-axis) and 7–9 $\mu m\, m^{-1}\, °C^{-1}$ (c-axis) in the temperature range of 25 °C (reference temperature) to 150 °C [9]. Hence, at a temperature of 150 °C, the volumetric thermal expansion is approximately 0.5%. At ambient temperature, the thermal strains are negligible compared to RIVE. The exact temperature during ion irradiation must be determined by a heat transfer analysis using radiation-induced energy deposition as a heat source. Experimental measurement of the surface temperature during irradiation seems to indicate minimal temperature increase.[†].

4.4.2 Phase Transition

Phase transitions occur at specific pressures and temperatures, and because they affect the crystalline structures of the minerals, their physical properties are affected. Notably, phase change can lead to density change, such as $\alpha \rightarrow \beta$ transition of quartz (low to high): $\rho_{\alpha-\mathrm{Qz}} = 2.65\ \mathrm{g\,cm^{-3}} \rightarrow \rho_{\beta-\mathrm{Qz}} = 2.533\ \mathrm{g\,cm^{-3}}$ occurring at 573 °C at ambient temperature and increasing linearly with increasing pressure (approximately 800 °C at 1 GPa). This mechanism is thus unlikely to occur under ion irradiation.

4.4.3 Crystalline Plasticity

At ambient temperature, most rocks exhibit a brittle elastic behavior. At high temperature and pressure, rock-forming minerals exhibit crystalline plasticity and viscous-brittle transition [7]. As mentioned earlier, previous studies have hypothesized the possibility of ion irradiation–induced viscous or plastic flow [25, 5, 6]. The mechanism of irradiation-induced assisted viscous or plastic flow is not elucidated at this stage, so only hypotheses can be proposed. It can be hypothesized that the ion- or irradiation-ballistic effects weaken cleavage planes and promote slippages under high stresses. If that hypothesis were to be validated, then this effect would be predominant in ion irradiation experiments which cause large stresses. This phenomenon was detailed in Section 4.3.

[†]Private communication with Pr. Murakami (U. of Tokyo).

5. IRRADIATION-INDUCED FLOW

As mentioned above, the main observation is that almost all RIVE is redirected in the vertical direction. The high planar stress state resulting from the dpa profile nonuniformity, as well as the presence of structural restraints of the irradiated layer, are the causes for such induced stresses. The observed redirection of the deformation that is a function of the stresses may be explained by the following irradiation-induced flow hypothesis, which must be tested computationally:

H 1 Ion- or irradiation-ballistic effects weaken cleavage planes and promote slippages under high stresses.

5.1 PLASTICITY-BASED MODEL

Given the very limited experimental data that can be used to calibrate a detailed plasticity model, a simple von Mises plasticity constitutive model with RIVE-dependent yield strength damage was developed. The stress tensor $\boldsymbol{\sigma}$ is related to the elastic strain tensor through the fourth-order elasticity tensor $\mathbf{C}$, as in Eq. (8),

$$\boldsymbol{\sigma} = \mathbf{C} : (\boldsymbol{\varepsilon} - \boldsymbol{\varepsilon}^p - \boldsymbol{\varepsilon}^*) \tag{8}$$

where $\boldsymbol{\varepsilon}$, $\boldsymbol{\varepsilon}^p$, and $\boldsymbol{\varepsilon}^*$ are the total, plastic, and imposed RIVE strain tensors, respectively.

For typical Von-Mises plasticity with isotropic strain hardening (or even strain softening), the yield function can be written as

$$f(\boldsymbol{\sigma}, \kappa) = \sqrt{3J_2} - h(\kappa), \tag{9}$$

where J_2 is the second invariant of the deviatoric stress tensor and $h(\kappa)$ is a function of the uniaxial yield strength of the material f_y that represents how the yield surface expands (in hardening) or contracts (in softening) as a function of a measure of the plastic strain (typically the effective plastic strain). However, in the most simplified model presented here, the only consideration is that the material microstructure will soften as a function of the degree of amorphization as a result of irradiation, which is considered to be linearly proportional to the magnitude of the imposed RIVE $\boldsymbol{\varepsilon}^*$. In its simplest form, such a softening damage would be linear with a constant κ as a free model parameter. However, some data suggest that the elastic modulus of irradiated aggregate minerals tends to decay exponentially as a function of $\boldsymbol{\varepsilon}^*$. In addition, f_y itself is not clearly defined and should also be considered as a free parameter to be identified by matching experimental data. Therefore, it was decided to fix the dependence relationship assuming that the pristine f_y^0 would degrade with the same degree as the modulus of elasticity as a function of $\boldsymbol{\varepsilon}^*$ using the same exponential decay function as $f_y = f_y^0 \exp(-\kappa\|\boldsymbol{\varepsilon}^*\|)$. Thus, the yield function is defined by Eq. (10) as

$$f(\boldsymbol{\sigma}, \kappa) = \sqrt{3J_2} - f_y^0 \cdot \mathrm{e}^{-\kappa\|\boldsymbol{\varepsilon}^*\|}, \tag{10}$$

where κ here is the exponential decay coefficient assumed to be $52.8{\times}10^{-2}$ [13]. This allows f_y^0 to be a free model parameter that can be calibrated by matching the evolution of step height of ion-irradiated samples.

In this model, isotropic behavior is assumed because the materials to be simulated are polycrystalline, so on average, they would exhibit isotropic behavior, even though they are typically anisotropic at the crystal level.

5.2 GEOMETRY AND INPUTS FOR THE SIMULATION OF ION IRRADIATION

The experimental data to be simulated are relevant to the irradiation of quartz discs that are 12 mm in diameter and 2 mm thick. Copper/molybdenum masks were used to expose two rectangular windows both measuring $2.5 \times 5.0mm$ on the sample's surface. Both windows were irradiated by Si^{2+} ions up to a fluence of 10^{15} Si/cm^2, and then only one window was further irradiated up to a fluence of 10^{16} Si/cm^2. Two irradiation energies were used—2 MeV and 10 MeV—for each fluence level. Thus, four irradiation conditions per material were achieved. Figure 2 shows the SRIM-calculated dpa profile for each case.

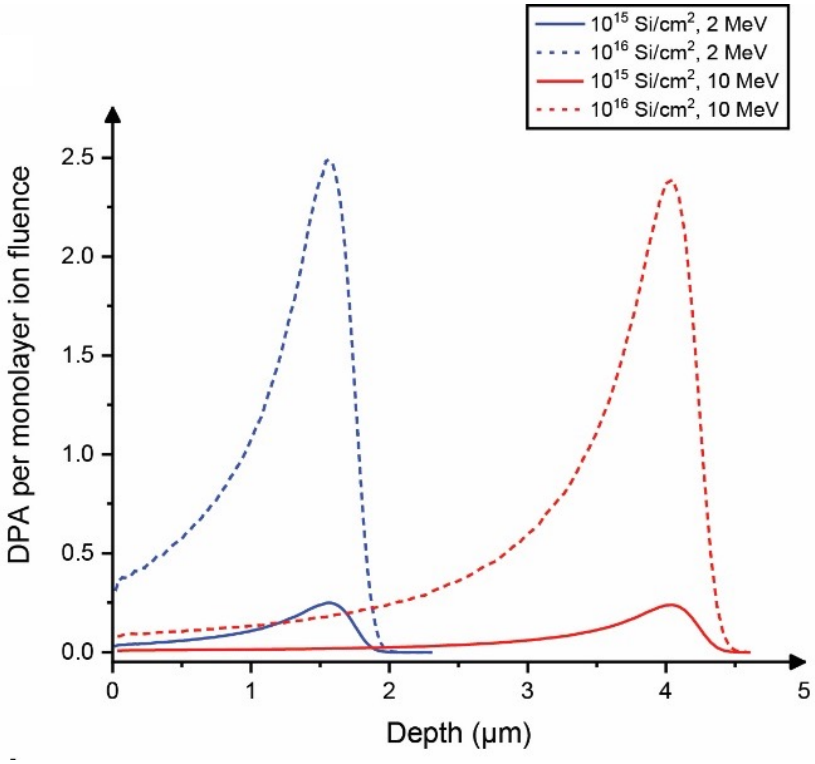

Figure 2. dpa profile under different irradiation energies and fluences computed using SRIM simulations.

Because the dpa profile varies over a very thin layer of the material ($< 5\ \mu$m), a nonuniform discretization in the vertical direction is inevitable. Additionally, the mesh size in the substrate was also significantly coarser compared to that of the element thickness. Coarsening the mesh size is necessary to achieve reasonable computational cost. However, as a result, the deformations and stresses around the boundaries are not very accurate, but the results will provide a measure of their actual magnitude. Furthermore, to save computational cost, symmetry about both x and y axes was assumed. Figure 3 shows the full and reduced mesh in plan view, presenting the symmetry boundary conditions and the vertical mesh details.

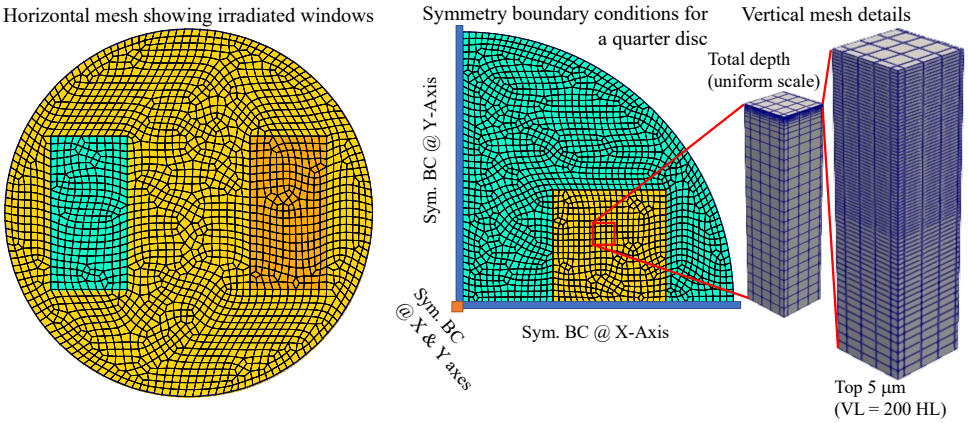

Figure 3. Full mesh of the irradiated disc (left), mesh for one quarter of the disc showing symmetry boundary conditions (middle), and mesh refinement over depth (right).

5.3 DISCUSSION OF SIMULATION RESULTS

As mentioned above, the purpose of this simulation is to shed light on the interdependencies and interactions between mechanical restraints and RIVE caused by ion irradiation. The main interactions arise from restraints from the nonirradiated material which lead to changes in the stress state within and at the boundaries of the irradiated thin film. This induces very high stresses as RIVE evolves. In turn, such stresses are assumed to induce plastic flow that is also a function of the degree of amorphization. Other geometrical parameters also have some effects that are elucidated herein, along with additional proposed possible interactions. In the following sections, the x and y axes are defined relative to the plate, as shown in Figure 3.

5.3.1 Boundary Restraints from the Nonirradiated Material

As shown in Figure 3, the irradiated material (within each exposed window) is surrounded on all four sides. In addition, ions penetrate down to a very thin thickness of less than 2 μm and 5 μm under 2 MeV and 10 MeV beam energies, respectively (see Figure 2). Thus, the irradiated material is a film that is fixed to the 1.995 1.998 mm thick substrate and is laterally constrained by at least 1 mm of material all around it. With these restraints, it can be safely assumed that the lateral deformation of the irradiated film is fully restrained from all four sides and the bottom. Therefore, all RIVE must be compatible at these boundaries, which forces the pristine material at all boundaries to undergo large deformations and to endure considerable triaxial stresses. As a result of these restraints, the irradiated film is put under very high triaxial stresses to balance the effects of the boundary stress conditions. The problem is fairly complex given the evolution of amorphization that occurs beneath the film's surface and progresses toward the top. Furthermore, amorphization-induced damage to the f_y changes the stress state considerably. Nevertheless, several observations can be made regarding the evolution of stresses, as shown in Figure 4 a, b, and c, which illustrate the stress profiles for σ_{XX}, σ_{YY}, and σ_{ZZ} at 4 fluences: 5×10^{14} ion.cm^{-2}, 1×10^{15} ion.cm^{-2}, 5×10^{15} ion.cm^{-2}, and 1×10^{16} ion.cm^{-2}.

As shown in the figure, at all irradiation stages, σ_{XX} is always equal to σ_{YY}, even though the window is rectangular with an aspect ratio of 2, which proves that the planar displacement is fully restrained. At early stages, all stress profiles are nonuniform and tend to be highest at the bulk of the amorphized zone, where

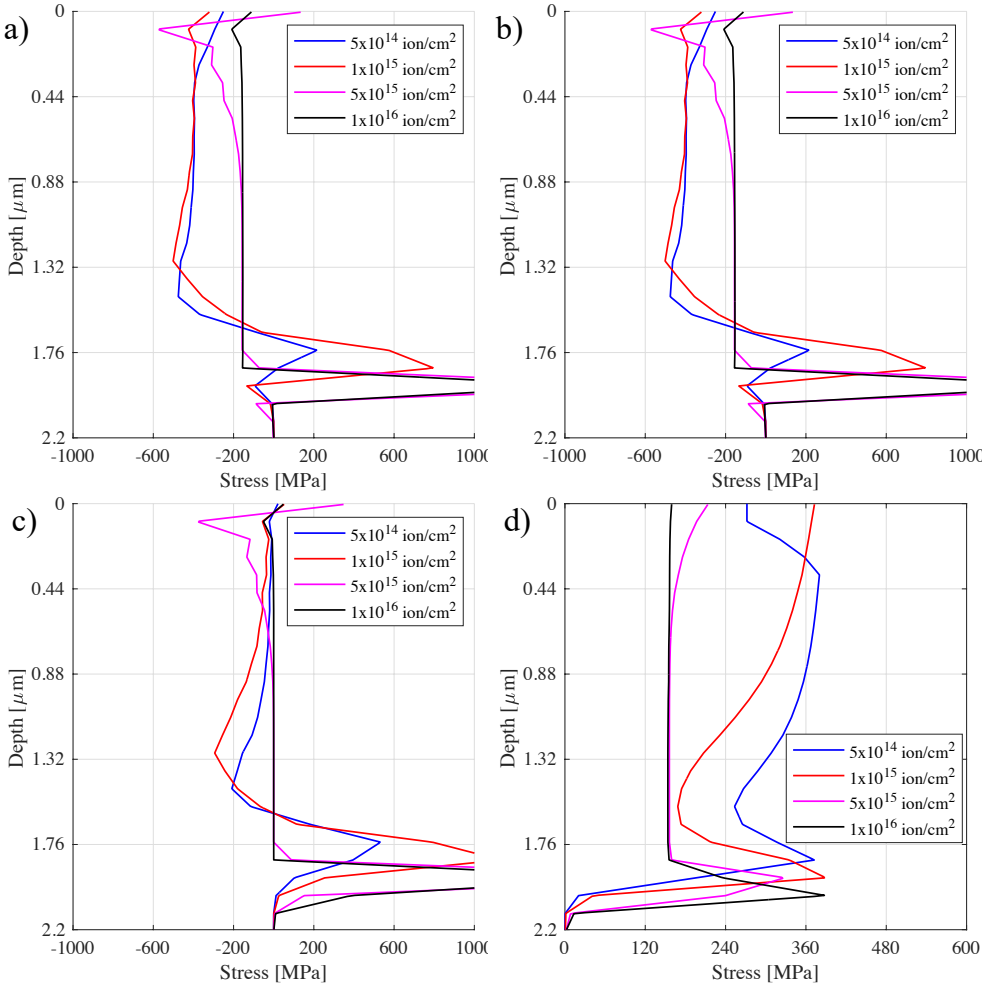

Figure 4. Stress distributions over the irradiated film depth: (a) σ_{XX}, (b) σ_{YY}, (c) σ_{ZZ}, and (d) σ_{VM}.

Von-Mises stress σ_{VM} is lowest in Figure 4d. At the bottom boundary, at the interface with the unirradiated material, σ_{ZZ} is higher than both σ_{XX} and σ_{YY}. However, at the free edge, it is lower because vertical confinement diminishes. At later stages, when most of the film is amorphized, the stress distributions all tend to be mostly uniform over the depth except for the two boundaries at the top and the bottom. In this case, σ_{ZZ} is close to zero. Thus, during amorphization, a net push toward the free surface is driven by σ_{ZZ} (because it is compressive), which, along with σ_{VM}, explains the observation that most of the deformation is in the upward direction. When the film is fully amorphized, this vertical compressive stress diminishes, with only the planar stresses remaining. This information will be used to explain the evolution of the step height in the following sections. These results are all expected, and they illustrate the complex interplay. The individual interaction trends are not the focus of this study, the significant interplay between mechanics and irradiation-induced deformation and expansion are significant. Another interesting observation pertains to the shear stresses close to the boundaries. Figure 5a shows a contour plot of σ_{ZX} on an X-Z section through the irradiated film (note that depth is scaled up to be visible). At any fluence, the stresses are very high at the interface. As a result, the irradiated window is surrounded by a ridge-like boundary as shown in Figure 5. This matches the experimental observations and further supports the irradiation-assisted flow hypothesis.

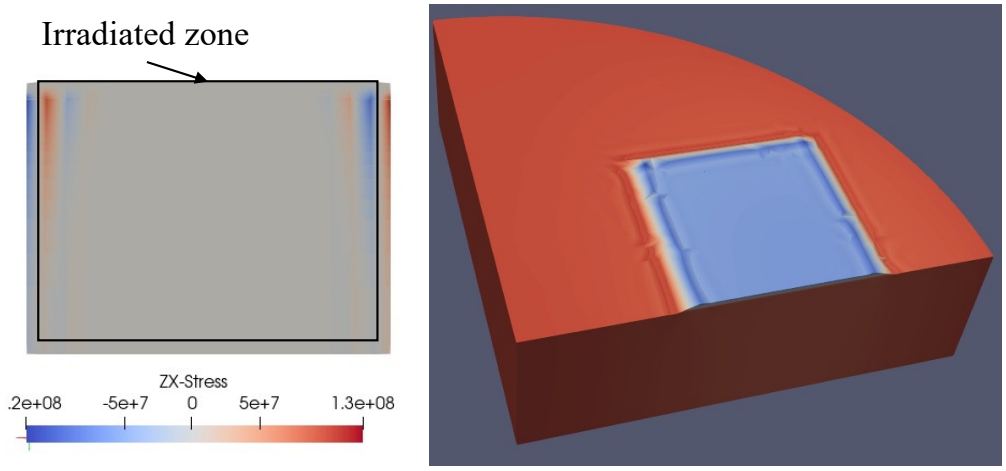

Figure 5. Shear stress over a vertical section through the irradiated film (left), and formation of ridges around the irradiated window (right).

5.3.2 Stress-Induced Plastic Flow

Stress magnitudes, even at very early fluences, are very high, reaching hundreds of MPa. At such very high planar stresses and with the existence of a much lower vertical stress σ_{ZZ}, it is quite probable that the material will flow along weak planes or near defects at various length scales, starting from the crystal structure itself up to the material grains and grain boundaries (GBs). The net result of such deformation is expected to be upward, even though RIVE of polycrystalline minerals has been shown to be mostly isotropic. In these simulations, **H 1** is partly tested by imposing RIVE isotropically and monitoring the resulting total strains. As can be seen in Figure 6, ϵ_{ZZ} asymptotically approaches the total RIVE value (not RIVE/3), whereas both ϵ_{XX} and ϵ_{YY} are almost equal to the imposed RIVE/3 value, but with a negative sign because of full restraint. This means that almost all $\boldsymbol{\varepsilon}^p$ is redirected in the vertical direction. Such confinement-induced flow redirection provides a very reasonable explanation of the observed experimental results, which indicate that almost all deformation is in the vertical direction: the total vertical deformation

is much closer to the RIVE and not RIVE/3.

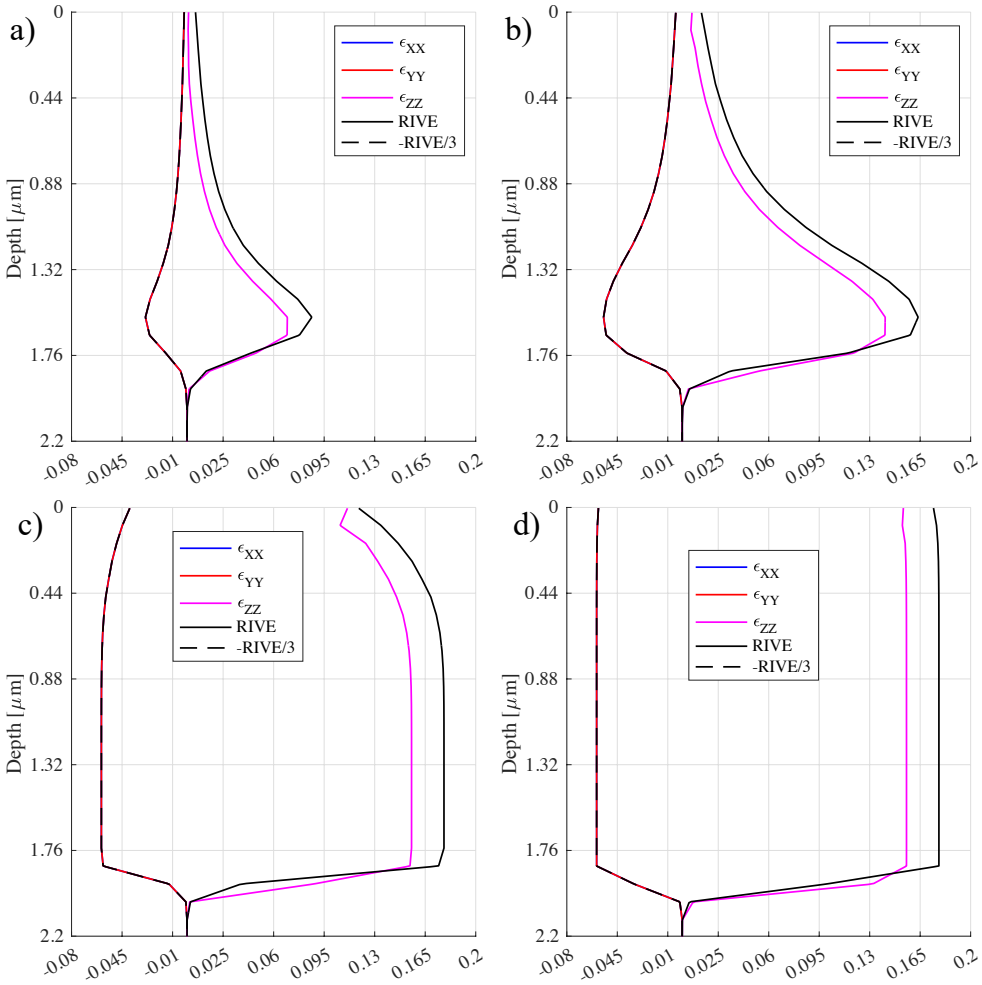

Figure 6. Strain distributions over the irradiated film depth: (a) ε_{XX}, (b) ε_{YY}, (c) RIVE, and (d) -RIVE/3.

5.3.3 Amorphization Effect on Yield Strength

It is important to note here that strain profiles in Figure 6 are relevant to an assumed f_y^0 = 400 MPa and κ =52.8×10^{-2}. Because there are no previously published yield strengths of rock-bearing minerals under irradiation, this parameter is an assumed value. However, changing this parameter allows for the complete testing of **H 1**. This testing is done by comparing the step height (Δh) evolution with RIVE and RIVE/3, as was previously theoretically done in Figure 1. Simply, the lower that f_y^0 is, the more rapidly Δh will deviate from the RIVE/3 trend line and asymptotically reach the RIVE trend line at a lower fluence. Additionally, the rate of change would also depend on the rate of f_y^0 damage, which is assumed to be an exponential function as explained above, given the very limited experimental data. Thus, to investigate the effects of f_y^0, four simulations were conducted. The parameters are obtained from the combinations of f_y^0 = 400 or 800 MPa with $\kappa = 52.8 \times 10^{-2}$ or 52.8×10^{-1}. The ranges of these parameters were chosen to assess their sensitivity on Δh trends. The results are presented in Figure 7. For all cases, beam energy was 2 MeV, and

temperature was 40 °C. As seen in the results, the expected trends are observed, and the results in general are in very good agreement with the experimental data plotted in Figure 1.

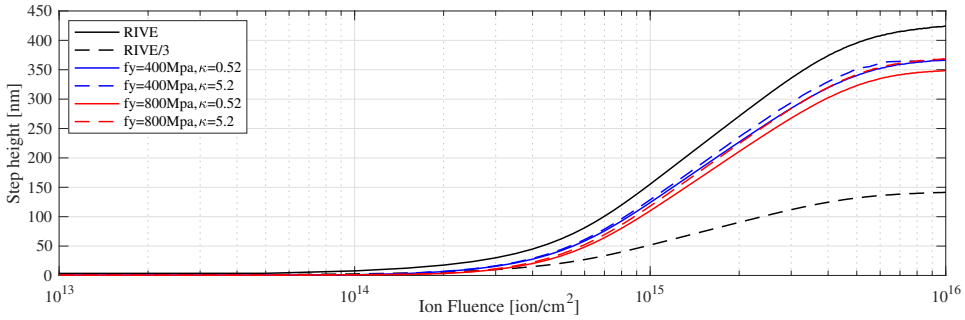

Figure 7. Step height obtained by integrating ϵ_{ZZ} over the height

5.3.4 Specimen Geometry

At the scale of the irradiated specimen, as RIVE increases, the irradiated film is subject to expansion pushing on the the substrate and creating expansion at the top surface. Therefore, it is expected that these forces will result in the curvature to the masking disk. Depending on the disc thickness, the curvature will be higher for thin discs and will continue to reduce as the disc becomes thicker. However, as the film amorphizes, its yield strength will drop down, thus reducing its pressure on the substrate. Thus, the curvature would decrease. Such a change in curvature was observed on thin plates of single crystal quartz [6]. In this work, a similar yet more complex deformation is observed. Figure 8 shows varied stages of the disk curvature when RIVE-induced amorphization increases. It can be observed that the peak difference of $120 - (-170) = 290$ nm occurs at about 6×10^{14} ion.cm^{-2}. However, the curvatures at all other values are all lower.

Such curvatures may affect the interpretation of step height from experimental measurements. Typically, the step height is measured by comparing the difference between the elevations over the irradiated and nonirradiated zones. Therefore, the area around the irradiation window plays a significant role in defining the datum. For example, in this simulation, the region around the irradiation window (excluding the irregular ridges at its edge) exhibits deformation in the range of -15 to 15 nm, so it can produce an error at around 30 nm (see Figure 9).

5.3.5 Possible Additional Interactions

Clearly, ion irradiation is accompanied by a significant amount of triaxial stresses. Therefore, the effects of confining pressure on the degree of amorphization and the expected RIVE values must be further understood. Additionally, for polycrystalline materials with interfacial zones between different mineral grains, higher interfacial stresses are expected to develop. Such stresses can promote further creep deformations and/or accelerate material dissolution at GBs. This stress-assisted corrosion mechanism may explain the observed increase in dissolution rates at GBs.

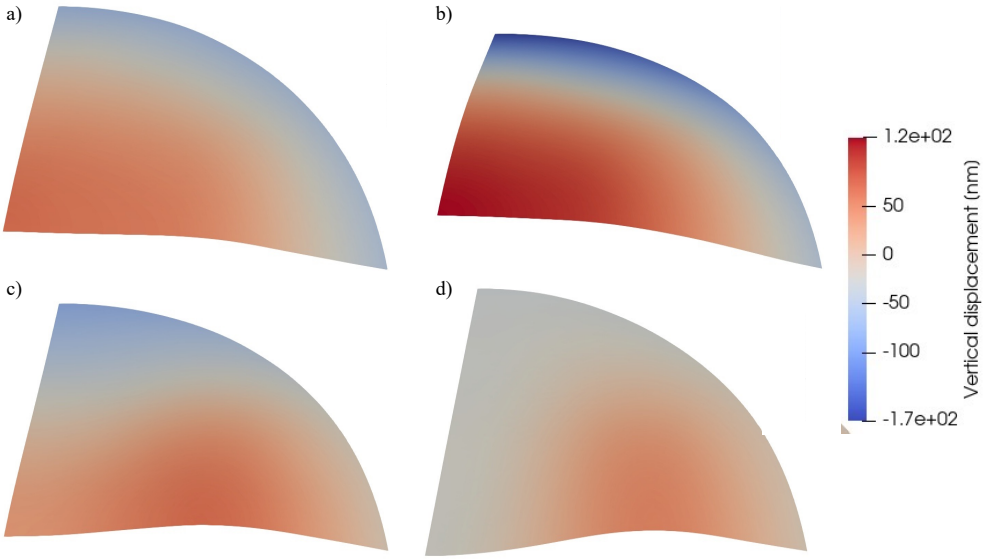

.

Figure 8. Bottom curvature at (a) 3×10^{14} **ion.**cm^{-2}**, (b)** 6×10^{15} **ion.**cm^{-2}**, (c)** 8×10^{15} **ion.**cm^{-2}**, and (d)** 1×10^{16} **ion.**cm^{-2}

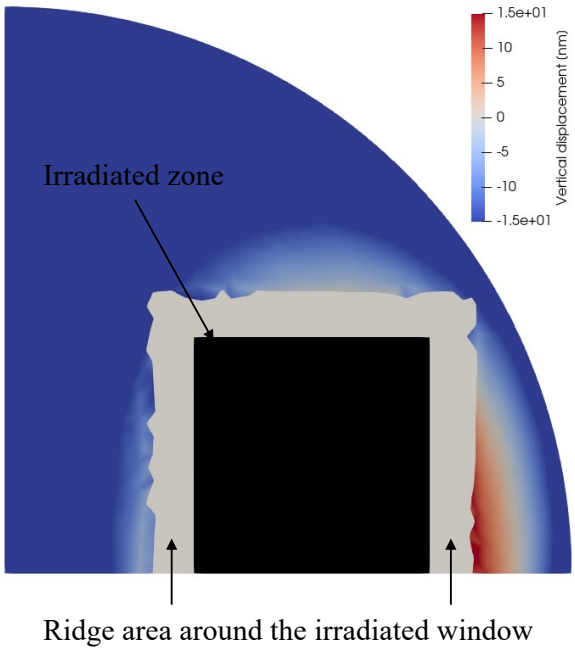

Figure 9. Top displacement around irradiated window.

6. IRRADIATION SIMULATIONS WITH MOSAIC

Based on the analysis presented above, it is clear that the irradiated material is restrained from lateral expansion, so it experiences significant lateral stresses and vertical stresses that are lower by orders of magnitude. The most important feature to be investigated at the microscale is the effect of the heterogeneity of the microstructure on the stress distribution. An acceptable approximation can be made by running MOSAIC simulations in 2D assuming full lateral restraints. Because the FEM simulations used homogeneous quartz data, direct one-to-one correspondence with MOSAIC simulations is not possible. However, the average planar stresses (σ_{XX} and σ_{YY}) from MOSAIC can be compared to those from the FEM simulations. In MOSAIC simulations, the vertical stress is zero, which represents a worst-case scenario because it is the lowest confinement case. If MOSAIC average stresses are within the same order of magnitude of those from FEM, then one can accept that MOSAIC local stresses resulting from heterogeneity of the microstructure are representative of the expected ion irradiation induced stresses. This simplified approach is utilized here.

6.1 PHASE MAPS

Two aggregate samples were simulated. Figure 10 shows the phase maps of an anorthite specimen and a granite specimen with the corresponding minerals. Both maps include different grain sizes of different phases with the presence of larger grains. Simulating the full map using MOSAIC is computationally expensive because the scanned area is large (25 mm × 50 mm), and the scans were obtained at high resolutions (2,476×1,224 pixels and 3,384×1,625 pixels for anorthite and granite, respectively). Therefore, these maps are virtually sliced along the vertical axis as shown in Figure 10 (slices to the right of each full map). The anorthite map was sliced into two slices of 1,238×1,224 pixels each, and the granite map was sliced into four slices 846×1,625 pixels each.

6.2 NEUTRON IRRADIATION

To simulate neutron irradiation, the studied slices are modeled assuming free expanding boundary conditions. The simulation results are presented in Figure 11 for anorthite (top) and granite (bottom), where principal stresses (σ_{max} and σ_{min}) and Von-Mises stress (σ_{VM}) are presented at the final stage (full amorhphization). In both specimens, tensile stresses around GBs are observed. Also, the amplitude of σ_{VM} is abnormally important because the analysis does not include damage effects. In reality, those tensile stresses will rapidly cause the formation of cracks and the relaxation of these high stresses.

6.3 ION IRRADIATION

As mentioned above, the studied slices are subject to full lateral restraint. The simulation results are presented in Figure 12 at full amorphization for the anorthite specimen (top) and the granite specimen (bottom), respectively. In both aggregates, no tensile stresses are developing, whereas significant compressive stresses are observed. Also σ_{VM} is significantly higher compared to results in the neutron case. The high compressive stresses around the small quartz inclusions may explain the pop-outs that were observed experimentally. The average boundary stresses for anorthite were -4.17 to -4.37 GPa, and those for granite were -2.46 GPa to -3.37 GPa. These microscale average stresses are within very close range to those from FEM simulations. MOSAIC simulations do not account for yield strength damage from irradiation, so σ_{VM} is expected to be higher than shown in the FEM results in the amorphized zones. By comparing the stress states in Figure 11 with those in Figure 12, it becomes apparent that neutron-induced

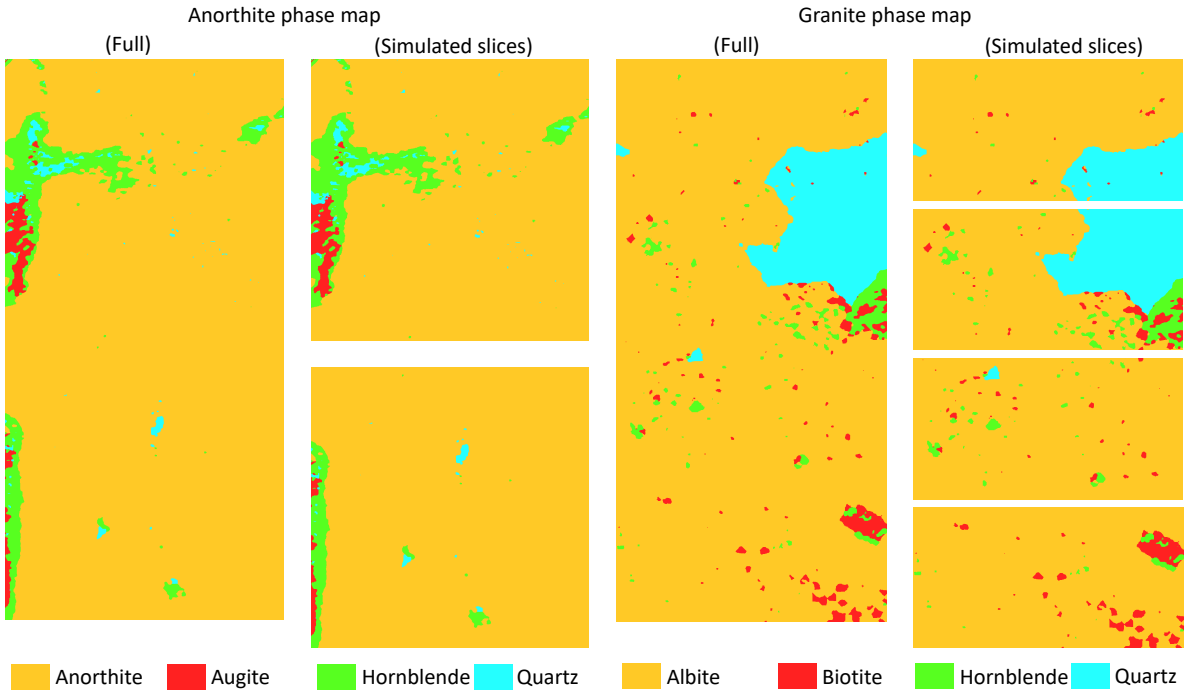

Figure 10. Phase maps of anorthite (left), and granite (right) specimens showing the slices used in MOSAIC simulations.

stress fields are significantly different than the corresponding fields caused by ion irradiation. Therefore, the damage mechanisms are expected to be very different, even if a correlation is found step-heights and the RIVE profiles. The very high compressive stress state in ion irradiation explains the lack of cracking in the examined samples.

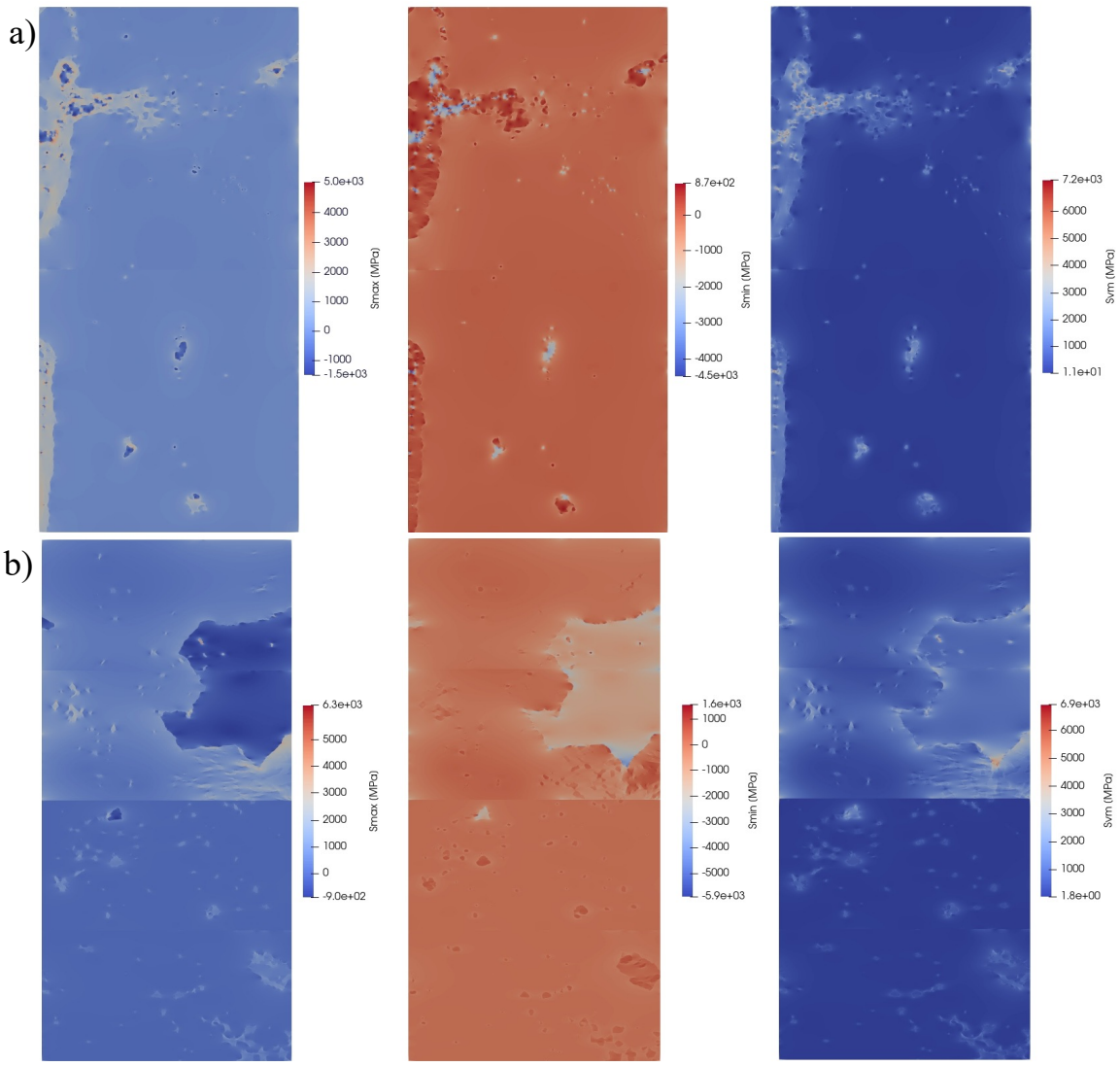

Figure 11. Elastic stress state within (a) anorthite sample and (b) granite sample at full amorphization with free boundary conditions to represent neutron irradiation: maximum principal stress (left), minimum principal stress (middle), and Von Misses stress (right).

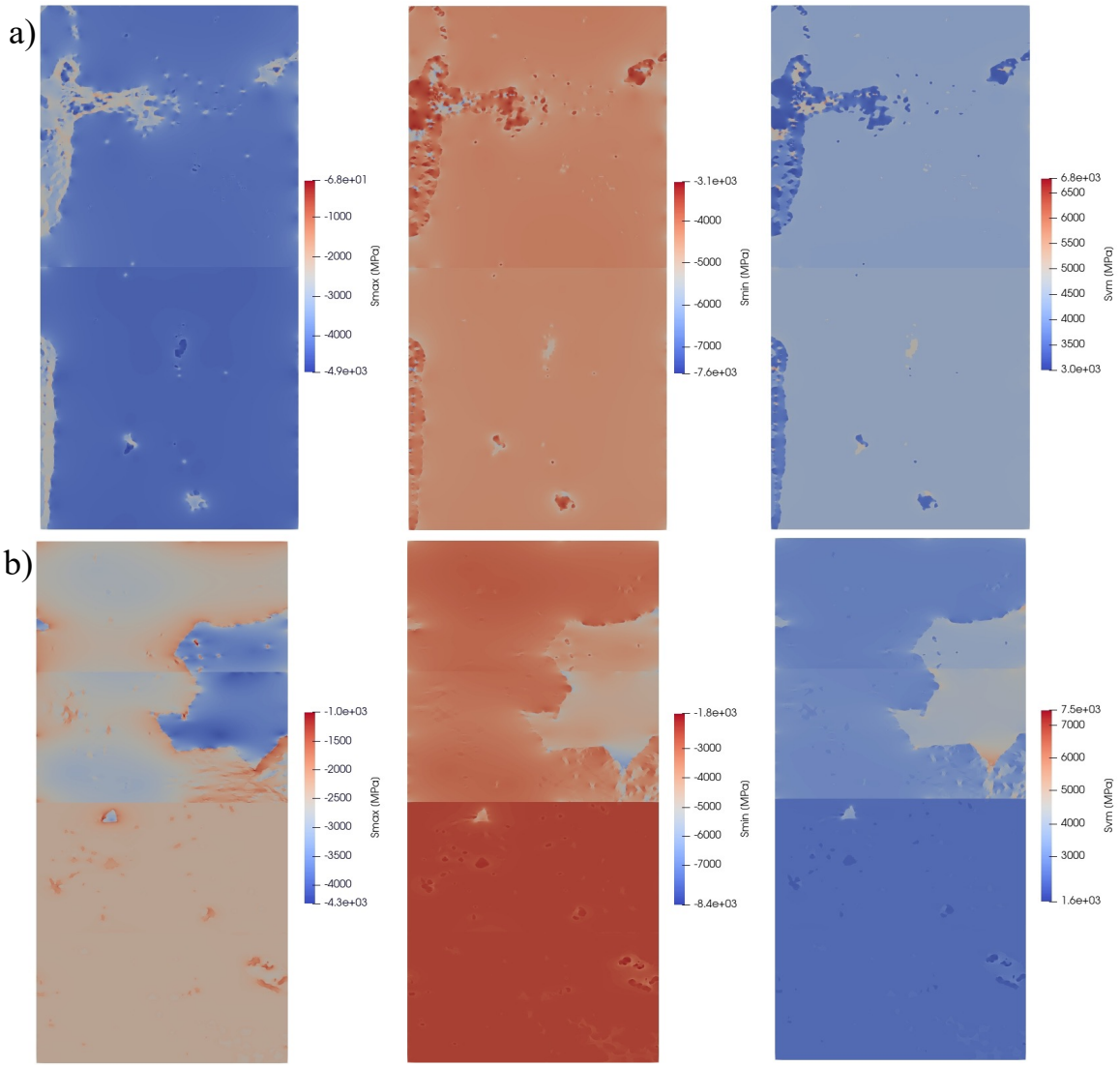

Figure 12. Elastic stress state within (a) the anorthite sample and (b) the granite sample at full amorphization with fixed boundary conditions to represent ion irradiation: maximum principal stress (left), minimum principal stress (middle), and Von Misses stress (right).

7. CONCLUSIONS

To support long-term operation and subsequent license renewals of the existing US LWR fleet, the risk of irradiation-induced degradation of the concrete structure shielding the neutron and gamma irradiation exiting the reactor pressure vessel must be assessed.

Unlike other nuclear components, structures made of concrete are built with local materials, so there is significant variability in the chemical compositions of natural aggregates used to build the nuclear concrete infrastructures. It is well established that the mineral composition greatly affects the tolerance of natural rocks against irradiation, with silicates being more sensitive than carbonates, for example.

Although the characterization of neutron-irradiated aggregates in test reactors remains the optimal approach to clearly establish the irradiation susceptibility of concrete forming aggregates, the experiment costs remain rather prohibitive for a large deployment. Alternatively, ion irradiation is a rapid, cost-effective means to achieve high doses of particle bombardment. The fundamental objective is to assess the representativeness of ion-irradiation analogues to model neutron irradiation. To make this assessment, this report presents the approach outlined below:

1. Establish a direct correspondence between neutron-radiation–induced volumetric expansion and ion RIVE using SRIM-based dpa profile.
2. Model the mechanical interactions occurring in the ion-implanted depth of minerals.
3. Establish that during ion irradiation, the development of large lateral stresses interfere with the RIVE and cause radiation-assisted (visco-)plastic flow.
4. Include a simplified plasticity model contribution to the constitutive law of irradiated minerals.
5. Use finite-element simulations to model the development of step height during ion irradiation.

The main conclusion of this analysis is that the apparent step-height underestimates the accumulated free RIVE in the ion-implanted depth by about 15% at full amorphization and about 25% toward the beginning of the ion irradiation experiment. The discrepancy is explained by the fact that the step height is proportional to the sum of the radiation-induced volumetric expansion (i.e., $\varepsilon^*/3$) and the plastic strains in the vertical direction ($< 2\varepsilon^*/3$). These results were obtained by finite element methods simulation.

Because of the large lateral compression stresses caused by the restraining effect of the unirradiated substrate, the stress field in the mineral grains and at the GB in the ion-implanted layer is much different than the comparable stress field occurring during neutron irradiation. Hence, the mismatch RIVE causing cracks in the rock-forming minerals leads to different patterns.

In conclusion, ion irradiation should only be considered as a partial surrogate method to neutron irradiation of concrete-forming aggregates. At the current stage of understanding and modeling, post–ion irradiation step-height measurement provides a direct assessment of the RIVE amplitude at its maximum extent. The kinetics of swelling (step-height as a function of dose) should be considered as an approximation of the RIVE kinetics under neutron irradiation.

To be able to fully understand the correspondence between ion- and neutron-irradiation, the following research should be undertaken:

- Study the mechanism of ion irradiation under mechanical constraint using molecular dynamics simulation to understand and characterize the irradiation-assisted (visco-)plastic flow.

- Develop a solid irradiation-assisted (visco-)plastic flow at the continuum scale of the minerals.
- Characterize the failure properties of rock-forming minerals under ion irradiation–induced multi-directional stress states.
- Implement the developed constitutive models on MOSAIC-3D to simulate both ion- and neutron-irradiation experiments.

8. REFERENCES

References

[1] V.N. Bykov, A.V. Denisov, V.B. Dubrovskii, V.V. Korenevskii, G.K. Krivokoneva, and L.P. Muzalevskii. Effect of Irradiation Temperature on the Radiation Expansion of Quartz. *Atomnaya Energiya*, 51(3):593–595, September 1981.

[2] A. Cheniour, Y. Li, J. Sanahuja, Y. Le Pape, E. Tajuelo Rodriguez, L.M. Anovitz, K.C. Polavaram, N. Garg, and T.M. Rosseel. FFT-Based Model for Irradiated Aggregate Microstructures in Concrete. *Materials and Structures*, 55(214), 2022.

[3] A.V. Denisov, V.B. Dubrovskii, and V.N. Solovyov. *Radiation Resistance of Mineral and Polymer Construction Materials*. ZAO MEI Publishing House, 2012. in Russian.

[4] K.G. Field, I. Remec, and Y. Le Pape. Radiation Effects on Concrete for Nuclear Power Plants – Part I: Quantification of Radiation Exposure and Radiation Effects. *Nuclear Engineering and Design*, 282:126–143, 2015.

[5] F. Harbsmeier and W. Boise. Ion Beam Induced Amorphization in Alpha Quartz. *Journal of Applied Physics*, 83(8):4049–4054, 1998.

[6] F. Harbsmeier, J. Conrad, and W. Bolse. Generation and Relief of Mechanical Stresses in Ion Irradiated SiC and SiO_2. *Nuclear Instruments and Methods in Physics Research Section B: Beam Interactions with Materials and Atoms*, 136-138:505–510, 1998. Ion Beam Analysis.

[7] J.E. Kendrick, Y. Lavallée, E. Mariani, D.B. Dingwell, J. Wheeler, and N.R. Varley. Crystal Plasticity as an Indicator of the Viscous-Brittle Transition in Magmas. *Nature Communications*, 8(1926), 2017.

[8] G.H. Kinchin and R.S. Pease. The displacement of atoms in solids by radiation. *Reports on Progress in Physics*, 18:1–51, 1955.

[9] J.A. Kosinski, J.G. Gualtereri, and A. Ballato. Thermal Expansion of Alpha Quartz. In *IEEE Forty-Fifth Annual Symposium on Frequency Control*, Piscataway NJ, 1991.

[10] N.M.A. Krishnan, R. Ravinder, R. Kumar, Y. Le Pape, G. Sant, and M. Bauchy. Density-Stiffness Scaling in Minerals upon Disordering: Irradiation vs. Vitrification. *Acta Materialia*, 166:611–617, 2019.

[11] F. Lavergne, K. Sab, J. Sanahuja, M. Bornert, and C. Toulemonde. Investigation of the Effect of Aggregates' Morphology on Concrete Creep Properties by Numerical Simulations. *Cement and Concrete Research*, 71:14–28, 2015.

[12] Y. Le Pape, M.H.F. Alsaid, and A.B. Giorla. Rock-Forming Minerals Radiation-Induced Volumetric Expansion – Revisiting the Literature Data. *Journal of Advanced Concrete Technology*, 16:191–209, 2018.

[13] Y. Le Pape, J. Sanahuja, and M.H.F. Alsaid. Irradiation-Induced Damage in Concrete-Forming Aggregates – Revisiting Literature Data through Micromechanics. *Materials and Structures*, 53:35, 2020.

[14] Y. Li, Y. Le Pape, E. Tajuelo Rodriguez, C.E. Torrence, D. Arregui Mena, T.M. Rosseel, and M. Sircar. Microstructural Characterization and Assessment of Mechanical Properties of Concrete Based on Combined Elemental Analysis Techniques and Fast-Fourier Transform–Based Simulations. *Construction and Building Materials*, 257(10):119500, 2020.

[15] V.N. Luu, K. Murakami, H. Samouh, I. Maruyama, T. Ohkubo, P.P. Tom, L. Chen, S. Kano, H. Yang, H. Abe, K. Suzuki, and M Suzuki. Changes in Properties of Alpha-Quartz and Feldspars under 3 MeV Si-Ion Irradiation. *Journal of Nuclear Materials*, 545:152734, 2021.

[16] I. Maruyama, O. Kontani, M. Takizawa, S. Sawada, S. Ishikawa, J. Yasukouchi, O. Sato, J. Etoh, and T. Igari. Development of the Soundness Assessment Procedure for Concrete Members Affected by Neutron and Gamma-Irradiation. *Journal of Advanced Concrete Technology*, 15:440–523, 2017.

[17] G. Mayer and J. Gigon. Effets des Neutrons Sapides sur Quelques Constantes Physiques du Quartz Cristallin et de la Silice Vitreuse. *Le Journal de Physique et le Radium*, 18:109–114, 1956.

[18] G Mayer and M Lecomte. Effet des Neutrons Rapides sur le Quartz Cristallin et la Silice Vitreuse. *Le Journal de Physique et le Radium*, 21(12):846–852, 1960.

[19] Norgett M.J., Robinson M.T., and Torrens I.M. A proposed method of calculating displacement dose rates. *Nuclear Engineering and Design*, 33(1):50–54, 1975.

[20] H. Moulinec and P. Suquet. A Fast Numerical Method for Computing the Linear and Nonlinear Mechanical Properties of Composites. *Compte Rendus de l'Académie des Sciences, Série H. Mécanique, physique, Chimie, Astronomie*, 318(11):1417–1423, 1994.

[21] H. Moulinec and P. Suquet. A numerical Method for Computing the Overall Response of Nonlinear Composites with Complex Microstructure. *Computer methods in applied mechanics and engineering*, 157(1):69–94, 1998.

[22] F.D. Murnaghan. The Compressibility of Media under Extreme Pressures. *Proceedings of the National Academy of Sciences*, 30(9):244–247, 1944.

[23] I. Pignatelli, A. Kumar, K.G. Field, B. Wang, Y. Yu, Y. Le Pape, M. Bauchy, and G. Sant. Direct Experimental Evidence for Differing Reactivity Alterations of Minerals following Irradiation: The Case of Calcite and Quartz. *Scientific Reports – Nature*, 6(20155):1–10, January 2016.

[24] Stoller R.E., Toloczko M.B., Was G.S., Certain A.G., Dwaraknath S., and Garner F.A. On the use of srim for computing radiation damage exposure. *Nuclear Instruments and Methods in Physics Research Section B: Beam Interactions with Materials and Atoms*, 310:75–80, 2013.

[25] E. Snoeks, A. Polman, and C. A. Volkert. Densification, Anisotropic Deformation, and Plastic Flow of SiO_2 during MeV Heavy Ion Irradiation. *Applied Physics Letters*, 65(19):2487–2489, 1994.

[26] C.E. Torrence, A.B. Giorl, Y. Li, E. Tajuelo Rodriguez, J.D. Arregui Mena, T.M. Rosseel, and Y. Le Pape. MOSAIC: An Effective FFT-Based Numerical Method to Assess Aging Properties of Concrete. *Journal of Advanced Concrete Technology*, 19(2):149–167, 2021.

[27] Saha Uttiyoarnab, Devan K., and Ganesan S. A study to compute integrated dpa for neutron and ion irradiation environments using srim-2013. *Journal of Nuclear Materials*, 503:30–41, 2018.

[28] K.H. Wedepohl. *Geochemistry*. Holt, Reinhart and Winston, 1971.

[29] J.F. Ziegler, J.P. Biersack, and M.D. Ziegler. *SRIM The Stopping and Range of Ions in Matter*.

[30] V.G. Zubov and A.T. Ivanov. Elasticity of Quartz Irradiated with Fast Neutrons. *Soviet Physics Crystallography*, 12(2):313–314, Sept.-Oct. 1967.